

Observing the universal screening of a Kondo impurity

C. Piquard,¹ P. Glidic,¹ C. Han,² A. Aassime,¹ A. Cavanna,¹ U. Gennser,¹ Y. Meir,³ E. Sela,² A. Anthore,^{1,4,*} and F. Pierre^{1,†}

¹*Université Paris-Saclay, CNRS, Centre de Nanosciences et de Nanotechnologies, 91120 Palaiseau, France*

²*Raymond and Beverly Sackler School of Physics and Astronomy, Tel Aviv University, Tel Aviv 69978, Israel*

³*Department of Physics, Ben-Gurion University of the Negev, Beer-Sheva, 84105 Israel*

⁴*Université Paris Cité, CNRS, Centre de Nanosciences et de Nanotechnologies, F-91120 Palaiseau, France*

The Kondo effect, deriving from a local magnetic impurity mediating electron-electron interactions, constitutes a flourishing basis for understanding a large variety of intricate many-body problems. Its experimental implementation in tunable circuits has made possible important advances through well-controlled investigations. However, these have mostly concerned transport properties, whereas thermodynamic observations - notably the fundamental measurement of the spin of the Kondo impurity - remain elusive in test-bed circuits. Here, with a novel combination of a ‘charge’ Kondo circuit with a charge sensor, we directly observe the state of the impurity and its progressive screening. We establish the universal renormalization flow from a single free spin to a screened singlet, the associated reduction in the magnetization, and the relationship between scaling Kondo temperature and microscopic parameters. In our device, a Kondo pseudospin is realized by two degenerate charge states of a metallic island, which we measure with a non-invasive, capacitively coupled charge sensor. Such pseudospin probe of an engineered Kondo system opens the way to the thermodynamic investigation of many exotic quantum states, including the clear observation of Majorana zero modes through their fractional entropy.

The Kondo model has proved to be an essential framework for the understanding and engineering of unconventional behaviors that develop in strongly correlated systems¹⁻⁴. It underpins current insights into a variety of promising phenomena, from the emergence of exotic non-abelian particles⁵⁻⁷ to heavy fermions^{1,4} and high- T_c superconductivity. The central element of this model is a local, energy degenerate ‘Kondo’ spin that effectively mediates interactions between itinerant electrons: As the temperature goes down, an initially weak antiferromagnetic coupling of the Kondo impurity with the spin of the electrons progressively grows, thereby giving rise to strong electron-electron correlations. The Kondo model and its variants are the continuing focus of huge body of theoretical^{8,9}, numerical¹⁰ and experimental works¹¹⁻¹⁶. While the complexity of bulk materials impedes the data-theory comparison¹⁷, a major step forward was made in 1998 with the experimental implementation in nanocircuits of tunable Kondo impurities, from two degenerate spin states of a quantum dot^{11,12}. However, experimental investigations of such Kondo circuits have essentially relied on their transport properties, which are inherently non-equilibrium quantities, whereas thermodynamic properties of primary interest remain elusive (see Ref. 18 for a charge compressibility measurement). In particular, due to the difficulty in measuring a single elementary magnetic moment, the spin of a Kondo impurity has not been possible to probe so far, in spite of its central role.

The present work overcomes this obstacle, demonstrates the universal screening of a Kondo impurity

and provides a thermodynamic window into the underlying many-body physics with a ‘charge’ pseudospin implementation¹⁹. As the role of the Kondo spin is here played by two charge states, it can be sensitively measured with a capacitively coupled detector²⁰⁻²³ (see Refs. 24, 25, 26 for first measurements of a ‘charge’ Kondo impurity). Such thermodynamic charge probe permits us to investigate the primary (1-channel) Kondo effect with ‘charge’ Kondo circuits. In contrast, with multiple contacts required for transport characterizations, a different physics emerges in these circuits²⁷⁻²⁹. One noteworthy challenge to achieve a full picture is the logarithmic spread of the Kondo crossover, which extends over many orders of magnitude in T/T_K with T_K the scaling Kondo temperature. Here, it is addressed through the particularly broad field-effect tunability of charge Kondo circuits, allowing for large variations of T_K . With this approach, we observe the crossover experienced by a Kondo impurity as the temperature T is lowered, from an asymptotically free (charge pseudo-) spin-1/2 to a screened singlet. The full Kondo screening is first evidenced from the saturation of the charge pseudospin susceptibility at low temperature. The complete universal crossover predicted by theory is then confronted with the temperature evolution of the Curie constant, which is considered to provide a measure of the effective spin³⁰. This comparison also informs on the relation between T_K and device parameters. Finally, we determine the screened Kondo (charge pseudo-) spin by measuring its fully polarized value, whose universal evolution is controlled by the ratio between Zeeman (charge states) energy splitting and Kondo temperature T_K .

The ‘charge’ Kondo mapping proposed by Matveev^{31,32} is implemented in the device shown in Fig. 1a. In this mapping, the local magnetic impurity

* e-mail: anne.anthore@c2n.upsaclay.fr

† e-mail: frederic.pierre@cnrs.fr

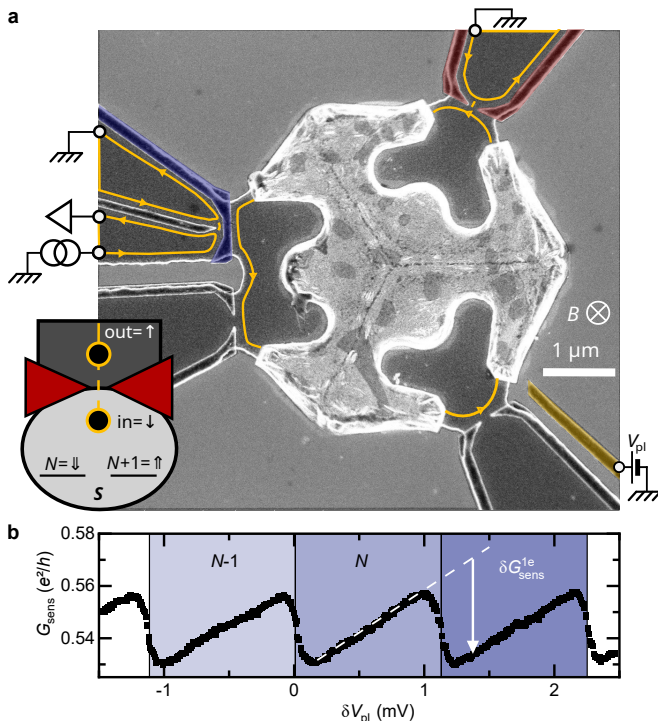


Figure 1. Metal-semiconductor charge Kondo device with a charge sensor. **a**, Colored e-beam micrograph of the measured device. A micron-scale metallic island (brighter) is connected through a tunable quantum point contact (QPC) formed by field effect using split gates (red, top-right) in a two-dimensional electron gas (2DEG, darker gray areas delimited by bright edges). The island’s charge Q is controlled with the plunger gate voltage V_{pl} (orange, bottom-right), and measured with a capacitively coupled sensor separated by a ‘barring’ gate (blue, left). The sensor consists of a constriction formed near the tip of the lateral gate (uncolored). The current propagates along the edges of the 2DEG set in the integer quantum Hall regime ($B \simeq 5.3$ T, filling factor $\nu = 2$), as depicted by orange lines with arrows (reflected inner channel not shown). A schematic (bottom-left) illustrates the charge Kondo mapping. **b**, Sensor calibration with a weakly connected island, implementing a single-electron box. The change δG_{sens}^{1e} in sensor conductance G_{sens} for an additional $1e$ charge is given by the periodic jumps when sweeping V_{pl} , which are associated with discrete increments in the mean number $\langle N_{isl} \rangle$ of electrons in the island. Source data are provided as a Source Data file.

of the original Kondo model is replaced by a Kondo pseudospin of $1/2$ ($S = \{\downarrow, \uparrow\}$) made of the two quantum charge states of lowest energy of a metallic island (bright central part), which can be tuned to degeneracy with a plunger gate voltage (V_{pl}). Such a reduction of the charge degree of freedom necessitates low temperatures and voltages with respect to the charging energy $E_C = e^2/2C$ (e the elementary electron charge, C the geometrical capacitance of the island), such that the other charge states are effectively frozen out. In practice, $E_C \simeq 39 \mu\text{eV} \simeq k_B \times 450 \text{ mK}$ thus sets a high energy cutoff for Kondo physics. The important role of the magnetic

field in the spin Kondo model is played by the detuning δV_{pl} from charge degeneracy. It induces an energy difference $2E_C \delta V_{pl} / \Delta$ (Δ the plunger gate voltage period) between the pseudospin charge states, which mimics the Zeeman splitting of a Kondo magnetic impurity. Whereas the Kondo model involves a spin-exchange interaction, the island’s charge (the impurity pseudospin) is not coupled to the real spin of electrons. Matveev instead introduced an electron localization pseudospin of $1/2$ ($s = \{\uparrow, \downarrow\}$) that labels wave functions according to their position, either within (\downarrow) or outside (\uparrow) of the island. This localization pseudospin description requires an effectively continuous electronic density of states in the metallic island (in contrast with small quantum dots with discrete energy levels). Failing that, an electron state outside of the island (\uparrow) could end up without a matching state of identical energy inside it, and thus no associated pseudospin (\downarrow). In this representation, each time an electron enters the island, both the island’s charge pseudospin \tilde{S} and the electron’s localization pseudospin \tilde{s} flip. This spin-exchange process coincides with the Kondo model (with an anisotropic coupling, as the irrelevant $S_z s_z$ coupling is absent³¹). The strength of the Kondo coupling is adjusted with a tunable quantum point contact (QPC, colored red) controlling the connection to the island, and characterized by the electron transmission probability τ across the QPC. Tuning the QPC to a larger τ increases the scaling Kondo temperature, thereby opening access to lower T/T_K . Note however that non-universal behaviors involving the high energy cutoff E_C might develop at high τ , upon reaching $k_B T_K \sim E_C$ (ultimately, at precisely $\tau = 1$, the charge quantization completely vanishes^{32,33} and there is no Kondo effect). Note also that the real spin of the electrons here constitutes a conserved quantum number effectively doubling the number of distinct electronic channels coupled to the metallic island. In practice, a strong magnetic field breaks the real spin degeneracy, in particular at the QPC, hence allowing to couple the spin-polarized electron channels one at a time. The primary (1-channel) Kondo effect of present interest is realized with a single electronic quantum channel (non-degenerate in real spin) connected to the island through the QPC.

The sample is nanofabricated on a Ga(Al)As heterojunction hosting a two-dimensional electron gas (2DEG) buried 90 nm below the darker surface delimited by etch-defined edges appearing bright in Fig. 1a. It is installed in a dilution refrigerator with heavily filtered and thermalized measurement lines³⁴, cooled down to an electronic temperature $T \simeq 9 \text{ mK}$ obtained from on-chip noise thermometry (Methods). It is also immersed in a strong perpendicular magnetic field ($B \simeq 5.3 \text{ T}$) corresponding to the integer quantum Hall effect at filling factor $\nu = 2$. In this regime the current propagates along two quantum Hall edge channels. The outer one is schematically shown as orange lines with arrows

indicating the propagation direction, while the irrelevant inner one, reflected at all QPCs, is not shown. This edge channel is in essentially perfect electrical connection with the thermally annealed AuGeNi metallic island, such that the Kondo coupling strength is entirely determined by the transmission probability τ across the single connected QPC (upper-right in Fig. 1a). Note that measuring τ requires us to connect additional channels to the island, as well as the application of a large dc voltage bias ($\sim 50 \mu\text{V} > E_C/e$) to minimize Coulomb effects (Methods). The two other QPCs controlled by uncolored metallic split gates are only used for characterization purposes and to establish the generic (QPC independent) character of our observations (Methods). Indeed, in contrast with the small quantum dot implementation of the Kondo model^{35,36}, multiple connected channels would compete to screen the charge Kondo pseudospin^{27,28,31,32}, a phenomenon with profound consequences described by another model referred to as multi-channel Kondo^{1-3,37}. For the data shown in the main manuscript, the path across each of these two other QPCs is disconnected.

The island's charge sensor consists in an additional QPC whose conductance G_{sens} changes by capacitive coupling with the electrical potential of the island. The sensor QPC is located along the 'barring' (separation) gate colored blue in Fig. 1a, near the tip of the uncolored gate. The 'barring' gate is negatively voltage biased to create a narrow depleted region providing a galvanic isolation (barring the way) between the sensor and the nearby edge channel emanating from the island. The conversion factor between a change in G_{sens} and a change in the island's charge can be straightforwardly calibrated with the connected QPC set to a weak, tunnel contact ($\tau \simeq 0.04 \ll 1$, the island then implements a single-electron box). In this tunnel regime and at low temperatures $T \ll E_C/k_B$, the mean number of electrons in the island $\langle N_{\text{isl}} \rangle$ is quantized and periodically increases, one electron at a time, when raising V_{pl} . The amplitude of the corresponding periodic jumps observed in $G_{\text{sens}}(\delta V_{\text{pl}})$ (see Fig. 1b) hence provides the change $\delta G_{\text{sens}}^{1e}$ (vertical arrow) associated with the addition of one electron. Note that the charge probed by G_{sens} includes the linear electrostatic contribution of V_{pl} mediated by the island (a much smaller direct cross-talk contribution is separately measured and compensated for, Methods), which results in the usually observed saw-tooth shape of $G_{\text{sens}}(\delta V_{\text{pl}})$ instead of a Coulomb staircase (see e.g. Ref. 26). The difference δN_{isl} in the mean number of electrons in the island with respect to the charge degeneracy point ($\delta V_{\text{pl}} = 0$) is obtained from

$$\delta N_{\text{isl}} \equiv \langle N_{\text{isl}} \rangle(\delta V_{\text{pl}}) - \langle N_{\text{isl}} \rangle(0) = \frac{\delta G_{\text{sens}}}{\delta G_{\text{sens}}^{1e}} + \frac{\delta V_{\text{pl}}}{\Delta}, \quad (1)$$

with $\delta G_{\text{sens}} = G_{\text{sens}}(\delta V_{\text{pl}}) - G_{\text{sens}}(0)$, and Δ the period in V_{pl} . At $|\delta V_{\text{pl}}| < \Delta/2$, the mean value of the charge Kondo pseudospin is simply given by $\langle S_z \rangle = \delta N_{\text{isl}}$. Interest-

ingly, despite the large geometrical difference with small quantum dots where this charge detection strategy was previously implemented²⁰⁻²³, we obtain a comparable conductance sensitivity per electron of $|\delta G_{\text{sens}}^{1e}| \simeq 0.04e^2/h$ (see Methods for checks with the sensor tuned to a larger sensitivity $|\delta G_{\text{sens}}^{1e}| \simeq 0.09e^2/h$). On the one hand, the larger geometrical capacitance of the metallic island results in a smaller voltage change e/C when adding one electron compared to a quantum dot, which by itself would reduce the sensitivity of the charge sensor. On the other hand, the larger island also results in a stronger capacitive coupling to the detector, which partially compensates for the lower voltage change. Moreover, the reduced impact of tuning the sensor on the bigger Kondo circuit compared to small quantum dots allows for a better detector optimization. In principle, for strong enough measurements, the charge sensor could interfere with the probed Kondo pseudospin, by projecting it. In practice, we avoid any discernible back-action notably by driving the sensor with a rather small ac voltage bias $V_{\text{sens}}^{\text{rms}} \lesssim 3k_B T/e$ (see Methods for specific tests and discussions).

In a preliminary step, we ascertain the charge detection procedure and validate that the device is described by Matveev's model where charge Kondo physics is predicted to develop. To this aim, we directly confront in Fig. 2 the charge measurements performed over a full plunger gate voltage period $\Delta \simeq 1.14 \text{mV}$ (symbols) with the quantitative analytical predictions (dashed lines) available for a connected QPC in the opposite tunnel ($\tau \simeq 0.04 \ll 1$, panel a) and near ballistic ($1 - \tau \simeq 0.015 \ll 1$, panel b) limits.

First, in the top panel (a), the displayed predictions correspond to the straightforward expression $\delta N_{\text{isl}} = \tanh(E_Z/2k_B T)/2$ for the statistical population of a pseudospin of $1/2$ in the presence of the effective 'Zeeman' splitting $E_Z = 2E_C \delta V_{\text{pl}}/\Delta$, to which is added the linear plunger gate contribution $-\delta V_{\text{pl}}/\Delta$ (see Eq. 1). Note that the charging energy $E_C \simeq k_B \times 450 \text{mK}$ and the electronic temperature $T \in \{9.4, 21.6, 30.4, 68.7\} \text{mK}$ are separately characterized (Methods), leaving no free parameters in the comparison. The match between data and theory shows, at our instrumental accuracy, that the sensor solely probes the island's charge, that additional charge states of the island can here be considered as frozen, and that the detector back-action is negligible even in this most sensitive tunnel configuration.

Second, in the bottom panel (b) addressing the near ballistic regime, the displayed theoretical prediction is a novel result obtained using Matveev's model of our device³², with a second-order perturbation treatment of the back-scattering amplitude $\sqrt{1 - \tau}$ valid at arbitrary $k_B T/E_C$ (see Supplementary Information for the derivation and full expression, see Eq. 4 in Methods for a $O(\pi k_B T/E_C)^2$ analytical prediction very accurate except at $T \simeq 69 \text{mK}$). A remarkable, parameter-free agreement is observed at $\tau \simeq 0.985$ (corresponding to a back-scattering amplitude of 0.12). This agreement quantitatively validates the charge measurement in the differ-

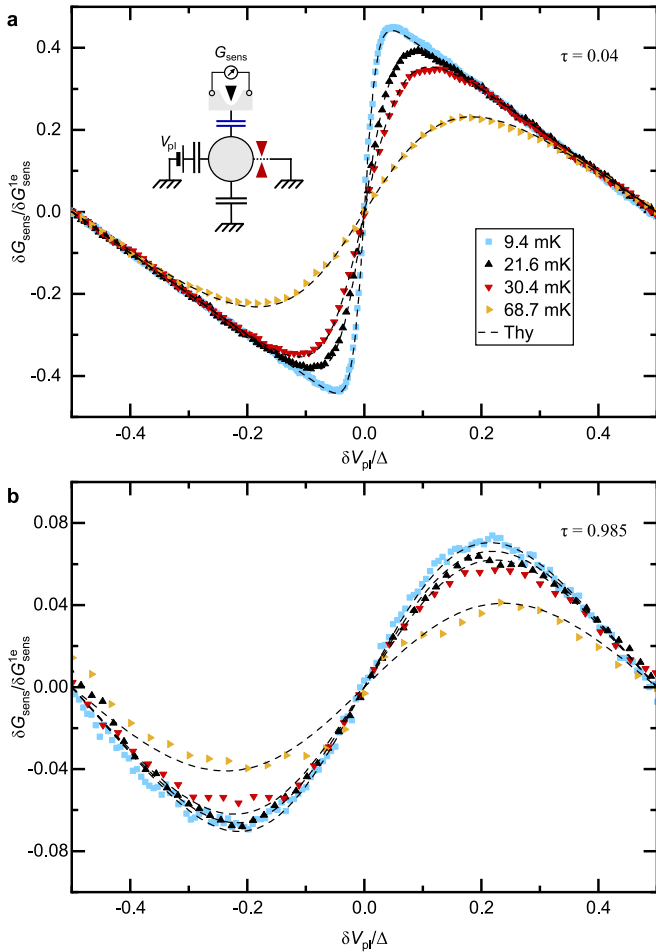


Figure 2. Charge sensing in tunnel and near ballistic limits. **a, b**, Sensor conductance signal plotted in $1e$ step units versus plunger gate voltage difference to charge degeneracy δV_{pl} in units of one period Δ . Each set of identical symbols correspond to data points at a distinct temperature T for a connected QPC set either in the tunnel ($\tau \simeq 0.04 \ll 1$, **a**) or near-ballistic ($1 - \tau \simeq 0.015 \ll 1$, **b**) limit. Measurements are plotted alongside the corresponding quantitative prediction (nearest black dashed line). Inset of **a** shows the circuit’s schematic. Source data are provided as a Source Data file.

ent device regime of an almost ballistic connection to the metallic island ($1 - \tau \ll 1$), where the island’s charge modulations are weak and hence relatively more sensitive to possible small artifacts such as nearby charged defects. Reciprocally, it also attests that the experimental device is adequately described by Matveev’s theoretical model at high τ , and in particular that the sensor back-action remains negligible. On these firm grounds the Kondo screening of the charge pseudospin is now explored.

A central feature of the 1-channel Kondo physics is that a spin-1/2 Kondo impurity becomes fully screened at low enough temperatures $T \ll T_K$. This can be demonstrated from the low-temperature behavior of the magnetic susceptibility χ of the impurity, since a finite

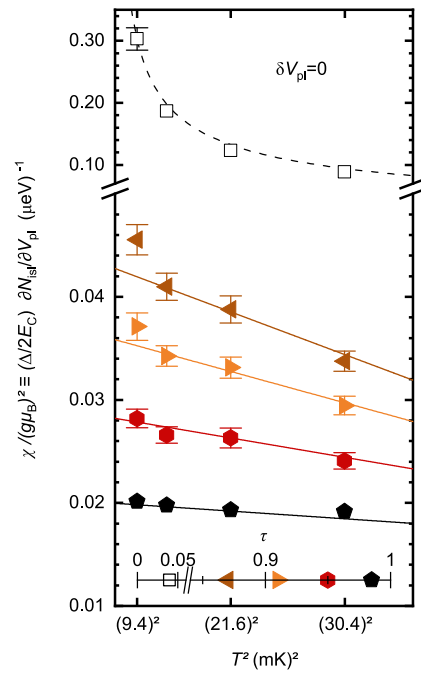


Figure 3. Screened charge Kondo pseudospin at strong Kondo coupling. The impurity charge pseudospin susceptibility measured at degeneracy ($\delta V_{\text{pl}} \simeq 0$) is plotted versus T^2 at $T < 40$ mK well-below the high energy cutoff $\sim E_C \simeq k_B \times 450$ mK. The continuous lines display the strong-coupling/near-ballistic quantitative predictions (τ -dependent, see Methods), converging as $\propto T^2$ toward a finite zero-temperature value. A non-diverging susceptibility as $T \rightarrow 0$ signals a fully screened pseudospin. The dashed line shows the weak-coupling/tunnel quantitative prediction $\propto 1/T$ for an asymptotically free impurity. The standard error is shown when larger than symbols. Source data are provided as a Source Data file.

(non-diverging) $\chi(T \rightarrow 0)$ implies a fully screened singlet ground state^{1,30}. We observe here such a screening signature of the charge Kondo pseudospin. In the present ‘charge’ implementation, the zero-field susceptibility $\chi/(g\mu_B)^2$ corresponds to $(\partial N_{\text{isl}}/\partial V_{\text{pl}}) \Delta/2E_C$ at $\delta V_{\text{pl}} \simeq 0$. Measurements of this charge Kondo susceptibility are displayed in Fig. 3 versus T^2 , where different symbols are associated with different Kondo couplings different τ ; see Supplementary Fig. 1. for χ displayed versus τ). In the weak Kondo coupling limit of a tunnel QPC ($\tau \simeq 0.04$, open squares), the susceptibility increases like $1/T$ when T is reduced (dashed line), as expected in the corresponding asymptotic freedom regime of an un-screened Kondo impurity ($T \gg T_K$, see Eq. 8 in Methods). In contrast, for the stronger Kondo couplings implemented through a higher QPC transmission ($\tau \gtrsim 0.9$), the susceptibility does not diverge but instead approaches a finite low temperature limit. This mere observation establishes the screening of the Kondo impurity predicted in the corresponding limit $T \ll T_K$. Quantitatively, the high transmission data closely match the parameter-free

predictions derived within Matveev's model of our device (straight continuous lines, Eq. 5 in Methods). The quadratic temperature scaling also corroborates the expected universal Kondo behavior at $T \ll T_K$ ¹. However, the universal character does not extend to the numerical value of the T^2 coefficient (although it obeys the specific predictions for our device), which could be attributed³⁸ to $k_B T_K$ being insufficiently small compared to the high-energy cutoff E_C for large τ (see Eqs. 5,7 and related discussion in Methods).

Beyond the screened and free Kondo impurity limits, we now extend our investigation to the full, universal renormalization flow as T/T_K is reduced. To this aim, we focus in Fig. 4 on the Curie constant, i.e. the susceptibility coefficient $T\chi$ (from dimensional scaling, χ without a prefactor T or T_K is not a universal function of T/T_K). For a free impurity, the Curie constant is directly related to its spin: $k_B T\chi/(g\mu_B)^2 = S(S+1)/3$ (0.25 for $S = 1/2$). More generally, the Curie constant is considered to provide a measure of the effective spin and, in particular, of the screened spin of the Kondo impurity³⁰. In the left panel (a), a representative selection of 'charge' $T\chi$ data, spanning a complete range of τ (see panel b for the distribution) is displayed versus $T < 40$ mK in a linear-log scale.

First, a log-like temperature dependence characteristic of the Kondo effect is evidenced from the near-linearity of the data, except at the lowest and highest $T\chi$. However, as each tuning of τ corresponds to a different value of T_K , each data set seems unrelated to the others when plotted versus T .

Second, the central panel (b) shows a comparison of the same data, now plotted vs T/T_K , with the universal curve for the standard spin Kondo model (1-channel, isotropic, $S = 1/2$) obtained combining a numerical calculation (continuous line, extracted from Ref. 8) and asymptotic predictions (dashed lines, see Eqs. 9 and 10 in Methods). To perform this comparison, the a priori unknown value of T_K must be fixed for each τ . In practice, we determine $T_K(\tau)$ such that, by construction, the data point at the lowest temperature ($T \simeq 9$ mK) lies on the predicted universal curve. The comparison in the main panel of Fig. 4b is then in the evolution as T is increased for each set of identical symbols. At our experimental accuracy, we observe a good match with the universal theoretical prediction, on an explored range extending over several orders of magnitude in T/T_K . Although T_K is a free parameter in the main panel of Fig. 4b, the underlying Kondo physics is stringently tested by further confronting this experimental $T_K(\tau)$ with predictions, see inset of b. The standard theoretical prediction for small couplings^{1,31} $T_K/E_C \propto \tau^{1/4} \exp(-\pi^2/2\tau^{1/2})$ is shown as a dashed blue line, and the prediction obtained expanding upon Matveev's model for high transmissions is displayed as a dashed red line (Eq. 6 in Methods). The data-theory agreement in the inset strengthens the comparison in the main panel, as the only fit parameter in the latter is seen to obey Kondo predictions in the

former. Note that at large τ , the Kondo temperature increases up to $k_B T_K/E_C \simeq 0.12$. Whereas non-universal deviations could develop, as pointed out in the previous paragraph, we find that they remain relatively small.

Third, for a direct, T_K -free comparison, the so-called β -function $\partial(T\chi)/\partial \log T$ vs $T\chi$, characterizing the universal renormalization flow of $T\chi$ is shown in Fig. 4c (continuous line) together with its analytical asymptotes (dashed lines, see expressions in Methods). Such β -function are broadly used in quantum field theory to describe the running of coupling constants under a renormalization group flow. Thanks to the logarithmic derivative, the energy scale T_K cancels out, and the universal character of the (monotonous) renormalization flow makes it possible to reformulate the dependence on T/T_K as a dependence on the renormalized quantity ($T\chi$). In practice, data points (symbols) are obtained by a discrete differentiation of measurements at the two closest temperatures for the same device setting of τ . As the experimental uncertainty on $T\chi$ ($\approx \pm 3\%$, see Methods) is to be compared with its relatively small change as the temperature is incremented, the scatter of individual data points is much broader in the β -function representation (Fig. 4c) than in the Curie constant representation (Fig. 4b). Nonetheless, the similitude between the data and the numerical Kondo prediction can here be most straightforwardly appreciated.

In contrast to the above susceptibility studies performed in the absence of a Zeeman-like energy splitting of the Kondo impurity ($E_Z \ll k_B T$), we explore here the pseudospin polarization $\langle S_z \rangle$ as the degeneracy between the two charge states is lifted (see Fig. 5). At large energy splitting with respect to the temperature ($E_Z \gg k_B T$), thermal fluctuations are suppressed and $\langle S_z \rangle$ corresponds to the partially screened spin of the impurity along a Kondo renormalization flow controlled by $E_Z/k_B T_K$. The universal Kondo prediction for $S_{\text{thy}}^{E_Z \gg T}(E_Z/k_B T_K)$ is shown as a continuous line in Fig. 5a³⁰. Representative measurement sweeps of $\delta N_{\text{isl}} \equiv \langle S_z \rangle$, each performed for a specific setting of τ and a fixed T , are plotted in Fig. 5a as a function of $E_Z/k_B T_K$ (thin dashed and dotted lines indicate, respectively, $T \simeq 9$ mK and 14 mK). Here $T_K(\tau)$ is not a free parameter, but the value separately obtained from the previous data-theory comparison on the Curie constant (see inset in Fig. 4b). Only a reduced E_Z interval of these measurement sweeps, highlighted with symbols, should be compared to the universal Kondo prediction. The highlighted E_Z interval is limited on the low side by the requirement of a sufficiently large $E_Z/k_B T$ ratio; in practice, we set the minimum value to 5. On the high side, the comparison to the universal Kondo prediction is limited to $E_Z \ll E_C$ (equivalently, $\delta V_{\text{pl}} \ll \Delta/2$), since other charge states are otherwise relevant, which breaks the Kondo mapping. In practice, we highlight $E_Z < E_C/5$ ($|\delta V_{\text{pl}}| < 0.1\Delta$). In this interval, as shown in Fig. 5a, a data-theory difference smaller than 0.04 is observed over the wide explored parameter range, for both $T \simeq 9$ mK and 14 mK (at higher temperatures there are no

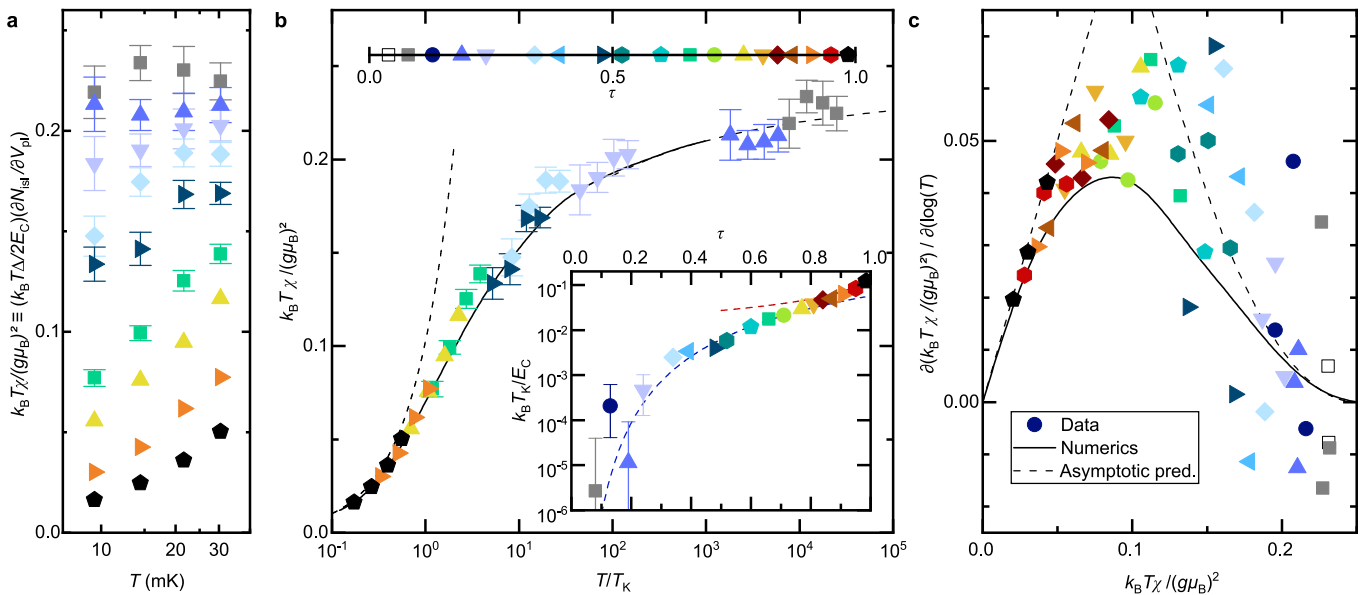


Figure 4. Universal temperature renormalization flow from free to screened Kondo spin, observed on the zero-field Curie constant (spin susceptibility coefficient) $T\chi$. Identical symbols (including in Figs. 3 and 5a) represent data points obtained for the same QPC setting (see b for correspondence symbol- τ) at different temperatures. Lines are universal predictions within the standard spin Kondo model (continuous: numerical calculations, dashed: asymptotic limits). The standard error is represented when larger than symbols, except in panel c where it can be inferred from the vertical spread of the data points. **a**, Measurements of $k_B T (\partial N_{\text{isl}} / \partial V_{\text{pl}}) \Delta / 2 E_C \equiv k_B T \chi / (g \mu_B)^2$ at $\delta V_{\text{pl}} \propto B = 0$ are plotted vs T in a linear-log scale. The (near) logarithmic behavior is indicative of the Kondo effect. **b**, The same $T\chi$ data points are plotted vs T/T_K , with $T_K(\tau)$ (see inset) obtained by matching with theory the $T \approx 9$ mK measurements. **c**, Parameter-free data-theory comparison on $\partial(T\chi) / \partial \log T$ vs $T\chi$, corresponding to the β -function characterizing the underlying Kondo renormalization flow. Source data are provided as a Source Data file.

data points fulfilling $5k_B T < E_Z < E_C/5$). We attribute this small discrepancy to the imperfect implementation of the theoretically considered limit of $k_B T \ll E_Z \ll E_C$. Note that although the experimental uncertainty on T_K can be important at very low $k_B T_K / E_C$ (see inset in Fig. 4b), it has little impact on the data-theory comparison, since $S_{\text{thy}}^{E_Z \gg T}$ is almost flat at the corresponding very large values of $E_Z / k_B T_K$. Hence, we experimentally establish here the predicted Kondo impurity magnetization vs $E_Z / k_B T_K$.

In a second step, we investigate the crossover from $\langle S_Z \rangle = 0$ to the above universal regime as $E_Z / k_B T$ increases, for a fixed $E_Z / k_B T_K$, which is expected to exhibit specific Kondo signatures markedly different from the polarization of a free spin⁸. For this purpose, we display in Fig. 5b the Kondo impurity magnetization $\langle S_Z \rangle$ normalized by the predicted universal value $S_{\text{thy}}^{E_Z \gg T}(E_Z / k_B T_K)$. Whereas for a free spin the crossover follows $\tanh(E_Z / 2k_B T)$ (dashed line), as $E_Z / k_B T_K$ is reduced a logarithmic broadening is predicted to develop with the Kondo effect (continuous lines)⁸. Data points shown as identical symbols and plotted in linear-log scale versus $E_Z / k_B T$ are measurements gathered from different settings of τ (and thus different T_K) and different Zeeman splittings whose ratio matches the same value of $E_Z / k_B T_K \in \{0.476, 0.952, 4.76\}$. As in panel a, the col-

lected data are limited on the high Zeeman splitting side to $E_Z < E_C/5$; however $E_Z / k_B T$ can be arbitrarily low. Similarly, we attribute the small discrepancy developing with E_Z to the imperfect implementation of the theoretically considered limit $E_Z \ll E_C$. The present observation hence establishes, without any free parameter, the unconventional Kondo crossover of a partially screened impurity from a thermally averaged-out polarization to a full polarization.

By implementing a single Kondo impurity with two charge states measured by a capacitively coupled sensor, we have directly observed the central Kondo spin as it progressively hybridizes with the conduction electrons. With this approach, we demonstrated the screening of the Kondo impurity and observed the universal crossover from asymptotic freedom to the strong coupling limit on a broadly tunable and fully characterized device. Such a thermodynamic probe of a Kondo impurity opens the way to exploring the quantum back-action of a detector on a many-body state, the impurity entropy of exotic quasiparticles^{23,39,40} or the entanglement negativity between Kondo impurity and electron bath⁴¹⁻⁴³. The present strategy can notably be applied to the large and continuously expanding family of Kondo-type models, hence providing a versatile platform to engineer and convincingly observe exotic states^{2,3,5,6,29}. In particular, the entropy associated with the charge Kondo impurity

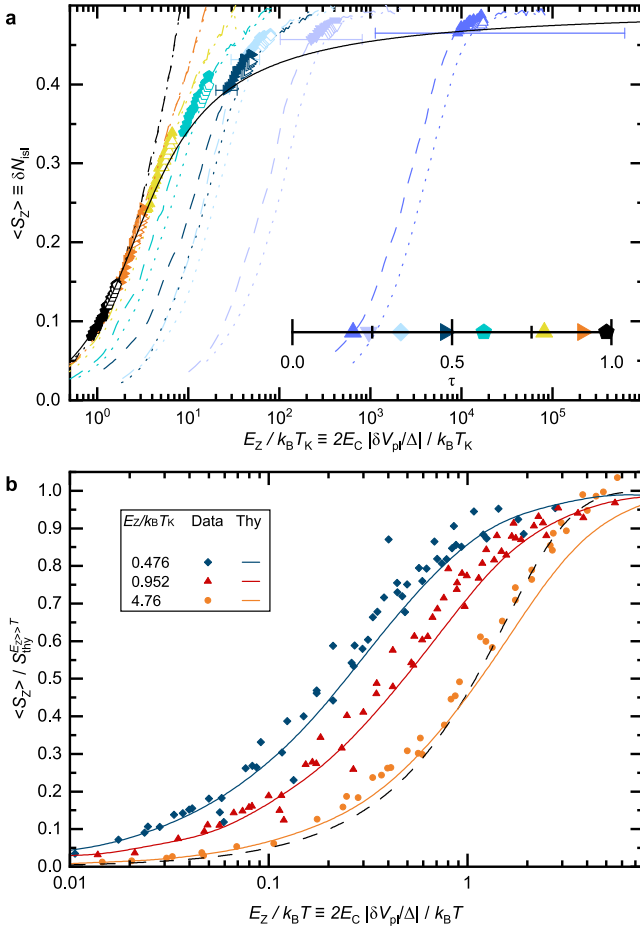


Figure 5. Kondo impurity magnetization. **a**, $\langle S_z \rangle \equiv \delta N_{\text{isl}}$ is plotted versus the ‘Zeeman’ energy splitting $E_Z \equiv 2E_C |\delta V_{\text{pl}} / \Delta|$ in units of the Kondo energy scale $k_B T_K$. The Kondo prediction $S_{\text{thy}}^{E_Z \gg T}(E_Z / k_B T_K)$, in the universal limit $E_Z \gg k_B T$ where it shows the transition from free to screened spin, is represented by a thick continuous line. Measurements at $T \approx 9$ and 14 mK are shown as dashed and dotted lines, respectively, with each color corresponding to a different τ (see inset in Fig. 4b for the separately obtained $T_K(\tau)$). Symbols (full for 9 mK, open for 14 mK) highlight data points for which a good agreement with the universal prediction is expected ($5k_B T < E_Z < E_C/5$). Horizontal error bars shown when larger than symbols represent the standard error dominated by the uncertainty on T_K . **b**, Progressive polarization of $\langle S_z \rangle / S_{\text{thy}}^{E_Z \gg T}$ with increasing $E_Z / k_B T$ at fixed $E_Z / k_B T_K$. The thermal crossover shifts and broadens with increasing $E_Z / k_B T_K$. Gathered data points restricted to $E_Z < E_C/5$ are shown as symbols. Kondo predictions are shown as continuous lines. The free-spin prediction $\tanh(E_Z / 2k_B T)$ is shown as a dashed line. Source data are provided as a Source Data file.

is predicted to take a fractional value of $k_B \log 2/2$ for the two-channel Kondo model. Such a measurement would provide a clear signature for the highly debated emergence of a free Majorana mode.

METHODS

Nanofabrication. The sample is patterned by standard e-beam lithography on a GaAlAs heterostructure forming an electron gas 90 nm below the surface, with a density of $2.6 \times 10^{11} \text{ cm}^{-2}$ and a mobility of $0.5 \times 10^6 \text{ cm}^2 \text{ V}^{-1} \text{ s}^{-1}$. The 2DEG mesa is delimited by a wet etching of approximately 100 nm in a $\text{H}_3\text{PO}_4/\text{H}_2\text{O}_2/\text{H}_2\text{O}$ solution. The ohmic contacts are realized with a metallic multilayer deposition of Ni(10 nm)-Au(10 nm)-Ge(90 nm)-Ni(20 nm)-Au(170 nm)-Ni(40 nm) followed by an annealing at 440°C where the metal penetrates the GaAlAs. Note that the active outer quantum Hall edge channel is found to be perfectly connected to the small metallic island at experimental accuracy (with a reflection probability below 0.1%). The gates forming the QPCs by field effect are made of aluminum deposited directly on the surface of the GaAlAs heterostructure.

Experimental setup. The measurements are performed in a cryo-free dilution refrigerator with extensive measurement lines filtering and thermalization. Details on the fridge wiring are provided in Ref. 44. Measurements of the conductance across the sample (for the device characterization) and across the charge sensor QPC are carried out with standard lock-in techniques at low frequencies, below 150 Hz, with ac excitations of rms amplitude below $k_B T/e$. Noise measurements for the thermometry described below are performed near 1 MHz with home-made cryogenic amplifiers⁴⁵.

Electronic temperature. The electronic temperature T is obtained from on-chip thermal noise measured on an ohmic contact. The conversion factor is calibrated from the linear slope of thermal noise vs temperature of the mixing chamber, at sufficiently high temperature where the difference between electron and mixing chamber temperatures is negligible. In practice, the calibration is performed above 40 mK where the high linearity of noise vs temperature attests of the good thermal anchoring of the electrons (here, differences between in-situ electronic temperature T and readings of RuO2 thermometers fixed to the mixing chamber develop essentially below 20 mK). The data displayed in the main manuscript are obtained at $T = \{9.4 \pm 0.3, 14.4 \pm 0.1, 21.6 \pm 0.2, 30.4 \pm 0.1, 46.2 \pm 0.1, 68.7 \pm 0.5\}$ mK, where the indicated uncertainties correspond to the temperature drifts occurring during the measurements.

QPC characterization. The Kondo coupling strength is controlled by the bare (unrenormalized) transmission probability τ across the connected QPC shown in Fig. 6. The value of τ is obtained by setting the two other QPCs (uncolored in Fig. 1a and normally closed) well within their broad transmission plateau and by applying a dc bias of $50 \mu\text{V}$ ($> E_C$ to suppress most of the dynamical Coulomb reduction of the conductance). The device resistance is then equal to the sum of the QPC resistance $h/\tau e^2$ and the well defined $h/2e^2$ resistance in series. Note that changing the tuning of the two other, normally closed QPCs impacts significantly, through capacitive cross-talk, the QPC of present interest. This effect can be calibrated and is mostly corrected for, as detailed below.

Capacitive cross-talk. The capacitive cross-talk that underpins the charge sensing mechanism also results in cross-correlations between the tunings of the different QPCs. Thanks to the distance of a few microns between constrictions

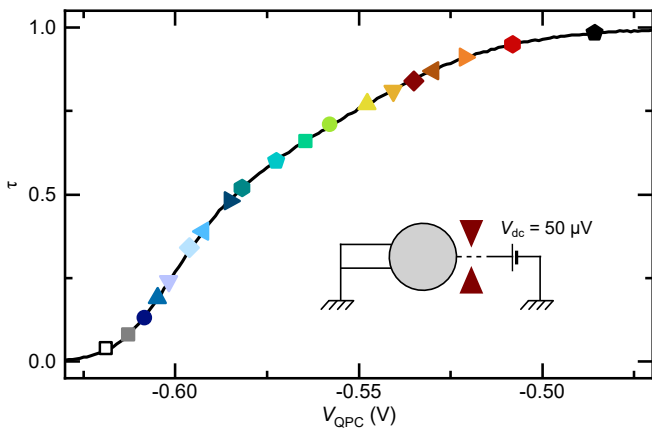


Figure 6. QPC characterization. Intrinsic transmission probability τ across the connected QPC vs applied voltage to the split gate. It is obtained from $\tau = 1/(e^2/hG - 1/2)$ with G the differential conductance of the device in the configuration shown in the schematic. Symbols represent the specific settings in the main manuscript. Source data are provided as a Source Data file.

tions, the influence of remote gates remains at a relatively small level of a few percent. Accordingly, the corresponding cross-talk can be mostly compensated for by relatively small, linear corrections calibrated separately, one pair of gates at a time. These corrections are employed for the determination of τ (see above in Methods), and also to maintain a charge sensor as stable as possible with respect to changes in the tuning of the QPC, as well as during sweeps in plunger gate voltage V_{pl} .

Charging energy. The experimental procedure to obtain the central charging energy $E_C \equiv e^2/2C \simeq 39 \mu\text{eV} \simeq k_B \times 450 \text{mK}$ combines two methods, performed with the device set to have two QPCs weakly connected to the island (see Fig. 7b).

In this single-electron transistor regime, we first measure the differential conductance across the device G_{SET} as a function of plunger gate voltage δV_{pl} and dc voltage bias V_{dc} . The height of the resulting Coulomb diamonds displayed in Fig. 7a corresponds to $2E_C$. The red continuous lines shows the diamonds boundaries for $E_C = 39 \mu\text{eV}$. Although very straightforward, the accuracy of this approach is mostly limited by the observed broadening of the diamond edges as V_{dc} is increased.

Second, the resolution on this central quantity is refined from the width of the G_{SET} peak at zero dc bias. In the asymptotic tunnel limit, where Kondo renormalization is ignored, theory predicts at $V_{dc} = 0$:

$$G_{\text{SET}}(\delta V_{pl}/\Delta) = G_{\text{SET}}(0) \frac{E_Z/k_B T}{\sinh(E_Z/k_B T)}, \quad (2)$$

with $E_Z = 2E_C \delta V_{pl}/\Delta$. As illustrated in Fig. 7c for the setting $\tau \simeq 0.04$ and $T \in \{9, 22, 46\} \text{mK}$, a very good match can be achieved between data (symbols) and Eq. 2. For each separately calibrated temperature a separate fitted value E_C^{fit} is extracted, shown in the panel d as open and full symbols for $\tau \simeq 0.04$ and 0.08 , respectively. These fitted values provide lower bounds for E_C since the residual Kondo renormalization slightly narrows the peak (by increasing the maximum conductance at degeneracy). The theoretical predictions for

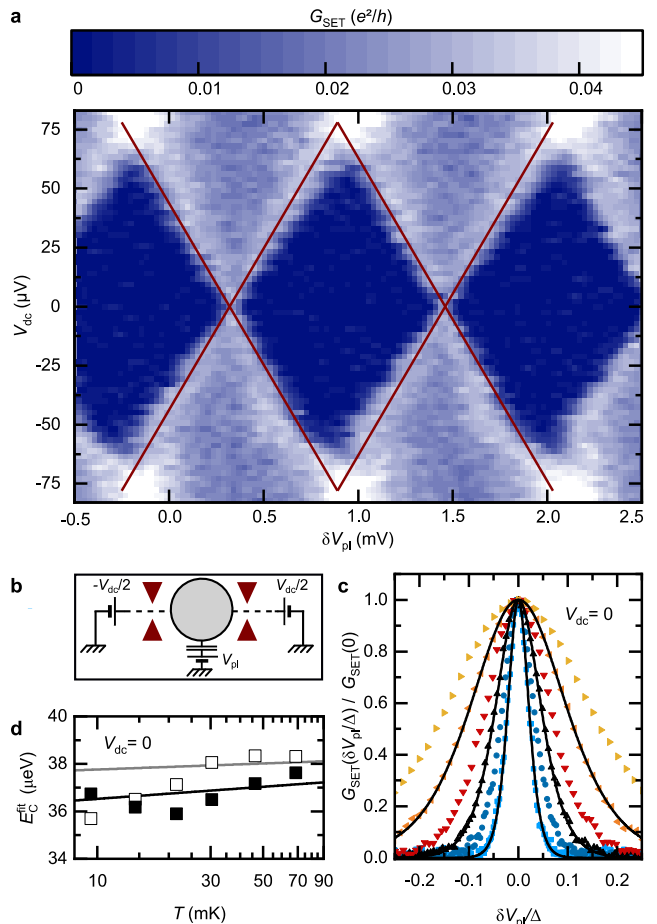


Figure 7. Charging energy extracted with the island connected by two QPCs, in the single electron transistor (SET) configuration schematically shown in b. Both QPCs are set to a small transmission probability. a, The differential conductance G_{SET} across the device is displayed on a color-map versus plunger gate voltage (δV_{pl}) and dc voltage (V_{dc}). The $E_C = 39 \mu\text{eV}$ prediction for the Coulomb diamonds edges is shown as red straight lines. c, The normalized conductance peak at zero dc bias (symbols, each color for a different T) can be fitted with the asymptotic tunnel theory (lines). The resulting E_C^{fit} are shown as symbols in d (open and full for, respectively, lowest and slightly higher QPCs transmissions). Lines in d represent the corresponding predictions for a fixed $E_C = 39 \mu\text{eV}$, also including the small Kondo renormalization effectively narrowing the peak (reducing E_C^{fit}). Source data are provided as a Source Data file.

the effective, Kondo renormalized E_C^* that is to be compared with E_C^{fit} is given, in the limit of tunnel contacts, by^{26,46}:

$$\frac{E_C^*}{E_C} = 1 - \frac{\sum \tau}{2\pi^2} \left(5.154 + \ln \frac{E_C}{\pi k_B T} \right) + O \left[\left(\frac{\sum \tau}{4\pi^2} \right)^2, \left(\frac{k_B T}{E_C} \right)^2 \right], \quad (3)$$

with $\sum \tau$ the sum of the transmission probabilities of all the channels connected to the metallic island (see Ref. 26 for a quantitative experimental observation). Grey and black lines in Fig. 7d show the theoretical predictions of Eq. 3 for E_C^* in the presence of two connected channels with the same transmission ($\sum \tau = 2\tau$) of, respectively, $\tau = 0.04$ and 0.08 , and using an unrenormalized charging energy of $E_C = 39 \mu\text{eV}$. We estimate our experimental uncertainty on the charging

energy to be of about $\pm 1 \mu\text{eV}$.

Charge data acquisition. The charge data are obtained from multiple repetitions of sweeps extending over several plunger gate periods. The displayed charge data within $|\delta V_{\text{pl}}| < \Delta/2$ are hence obtained from an ensemble of at least 30 measurements. As anomalies such as nearby charge jumps can affect the integrity of the measurements, several procedures are used to automatically discard suspicious data points or sweeps (in practice, less than 10%). 1) We first check the integrity of each one period sweep. For this purpose, we integrate with V_{pl} both the charge sensor conductance, as well as the absolute value of the difference between period sweep and reversed period sweep around the degeneracy point. Then we automatically discard each period sweep with a statistically anomalous integral value, defined in practice as being away from the mean by more than three times the standard deviation. 2) Second, we perform a separate statistical analysis for each individual value of δV_{pl} on the ensemble of corresponding data points from the remaining, preserved, one period sweeps. Specific data points away from the mean by more than three times the standard deviation are automatically dropped out before the final averaging is performed.

Experimental uncertainty. The displayed standard errors include the following independent contributions:

1) The measurement standard error, which is obtained from the statistical analysis of an ensemble of at least 30 independent data points. In practice, the standard error on sensor conductance is within $10^{-4} e^2/h$ and $2 \times 10^{-4} e^2/h$, with different specific values at different temperatures. For the susceptibility χ , each of the statistically analyzed data points correspond to an individual linear fit of the slope of the sensor conductance at the charge degeneracy point. In practice, the relative standard error on the susceptibility varies from 2% up to 8% in the most unfavorable cases.

2) The standard error on $\delta G_{\text{sens}}^{1e}$ (the sensor conductance change for an addition of one electron to the island). In practice, we find a standard error within 0.6% and 0.9% of $\delta G_{\text{sens}}^{1e}$ at $T \leq 30.4 \text{ mK}$. It increases up to 2% at 68.7 mK where the range of V_{pl} used to extract $\delta G_{\text{sens}}^{1e}$ (with a negligible thermal contribution) becomes a substantially reduced fraction of a period Δ .

3) The uncertainty on temperature of typically $\pm 3\%$ or less (see section ‘Electronic temperature’), which notably impacts the Curie constant $T\chi$ (comparably to the first, measurement standard error contribution on susceptibility).

The displayed standard errors in Figs. 3,4 include these independent contributions. In practice, we generally find that the overall standard error is similar to the scatter between displayed data points, except notably in Fig. 5 where the vertical scatter mostly results from the challenge in being simultaneously at $E_C \gg E_Z \gg k_B T$.

Reproducibility. The generic character of the results shown in this article is ascertained by checking their independence on (i) which specific QPC is connected to the metallic island, and (ii) the tuning of the charge sensor.

(i) We confront in Fig. 8a, the charge measurements performed at $T \simeq 9 \text{ mK}$ using individually each of the three physical QPCs to connect the metallic island (distinct symbols). For a direct comparison, the three QPCs are (one at a time) tuned to the same quantitative value of τ . Then we match the sensor conductance normalized by $\delta G_{\text{sens}}^{1e}$. For a more thor-

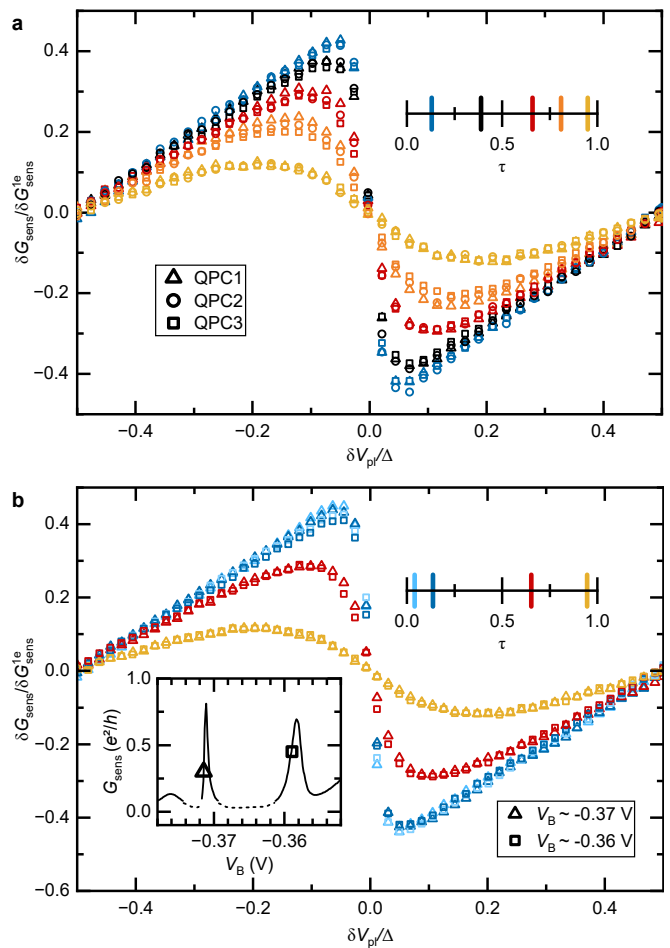


Figure 8. Reproducibility. The independence of the charge measurements on the connected QPC and on the charge sensor setting attests of the robustness and reproducibility of our results. **a**, Reproducibility with different connected QPCs. Measurements at $T \simeq 9.4 \text{ mK}$ of the sensor conductance signal in units of the $1e$ sensibility are plotted as symbols over one plunger gate voltage period. The different settings of τ (see color code) are each implemented on three different QPCs (different symbols) connected one at a time to the metallic island. **b**, Reproducibility with different charge sensor tunings. The charge measurements shown as symbols were repeated with two sensor settings, corresponding to different voltages V_B applied to the blue ‘barring’ gate (see inset for $G_{\text{sens}}(V_B)$, the dashed line for $G_{\text{sens}} \lesssim 0.1$ indicates a less reliable measurement). Squares correspond to the sensor setting used for the data in the main text, for which $\delta G_{\text{sens}}^{1e} \simeq 0.0375 e^2/h$. Triangles correspond to a more sensitive setting $\delta G_{\text{sens}}^{1e} \simeq 0.0937 e^2/h$. The normalized sensor signal at 9.4 mK is plotted versus $\delta V_{\text{pl}}/\Delta$ along with three different QPC transmission τ to the metallic island (see color code). Source data are provided as a Source Data file.

ough test, the comparison is performed over a full δV_{pl} period and for five representative values of τ spanning the full range from tunnel to ballistic (see scale bar for color code). The different symbols of the same color fall on each other, essentially within the symbols’ size, showing the QPC-independent character of our results. Note that small systematic differences most likely result from the uncertainty on the experimental values of τ .

(ii) The reproducibility of the charge measurement versus

charge sensor tuning is specifically checked in Fig. 8b. For this purpose, we confront the sensor conductance normalized by $\delta G_{\text{sens}}^{1e}$ obtained either with the main sensor tuning used for the data shown in the main text (open squares, $\delta G_{\text{sens}}^{1e} \simeq 0.0375 e^2/h$) or with a different, more sensitive tuning (open triangles, $\delta G_{\text{sens}}^{1e} \simeq 0.0937 e^2/h$) achieved with a more negative voltage applied to the ‘barring’ gate (see inset). The comparison is then repeated for three different settings of τ across the QPC connected to the island, over a full δV_{pl} period. The corresponding data points are nearly indistinguishable.

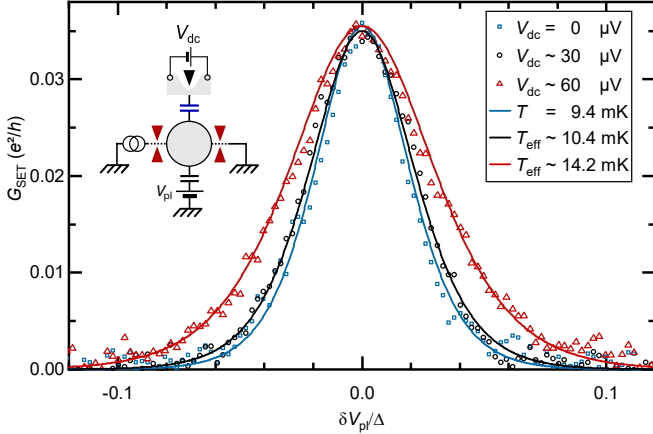


Figure 9. Charge sensor back-action vs dc bias. The conductance through the island in a SET configuration, with two connected QPCs in the tunnel regime (see schematic), is displayed as symbols versus $\delta V_{\text{pl}}/\Delta$ for different dc bias voltage V_{dc} applied to the charge sensor constriction, at $T \simeq 9.4$ mK. The peak width starts to broaden for a relatively large $V_{\text{dc}} \gtrsim 30$ μV . The displayed effective temperature T_{eff} are fits using the temperature as a free parameter. Source data are provided as a Source Data file.

Charge sensor back-action. The charge sensor can impact the probed charge Kondo physics through the back-action induced by the charge measurement. This phenomenon is more important for stronger measurements, and therefore for larger voltages applied to determine G_{sens} , as well as for larger tunings of the sensitivity $\delta G_{\text{sens}}^{1e}$. In practice, we probe the sensor conductance using a small ac voltage of rms amplitude smaller than $3k_{\text{B}}T/e$. Note however that, even at thermal equilibrium, the mere presence of a coupling to the charge sensor and/or the thermal fluctuations could be sufficient to perturb the probed system. In this section, we establish that the back-action can be neglected from (i) the negligible effect of increasing $\delta G_{\text{sens}}^{1e}$, (ii) the large bias voltage margin before the $1e$ charge step is broadened, (iii) the good fit of the charge step with the tunnel and near ballistic models ignoring the coupling to the sensor.

(i) We find that the charge data are indistinguishable when increasing by a factor of 2.5 the sensor $1e$ sensitivity, including in the most sensitive regime of a tunnel coupled island (see Fig. 8b). If the back-action was not negligible and controlled by the charge detector sensitivity, a difference should have developed.

(ii) We added a dc bias voltage to the small ac signal used to measure the sensor conductance to determine the back-action threshold. In practice, we chose to probe not the charge (the

charge sensor is impacted by the application of large biases) but the width of the peak displayed by the conductance G_{SET} across the island connected by two QPCs both in the tunnel limit (see schematic in inset). In this SET regime, the peak width of $G_{\text{SET}}(\delta V_{\text{pl}})$ is proportional to the temperature if the sensor can be ignored (and in the absence of other artifacts such as nearby charge fluctuators). We find at the most sensitive, lowest temperature $T \simeq 9$ mK that a dc voltage of nearly 30 μV applied to the sensor is required to induce a visible change in G_{SET} peak width (see T_{eff} values for the corresponding effective temperature). This is a much larger sensor drive than both the applied ac excitation amplitude of $2\mu\text{V}_{\text{rms}}$ and the thermal fluctuations $k_{\text{B}}T/e \simeq 0.8$ μV .

(iii) The quantitative, parameter-less match with theory ignoring the sensor back-action further establish that it is negligible. Such comparisons are shown in Fig. 2 for the measured charge, and in the good match between blue symbols and blue line in Fig. 9 for G_{SET} .

Charge Kondo circuit predictions at large QPC transmission. In this section we recapitulate the theoretical predictions at $1 - \tau \ll 1$ used to compare with the data. Their derivation is provided in the Supplementary Information.

The central new prediction, directly used in Fig. 2b, is the island charge in electron charge units $\delta Q/e \equiv \delta N_{\text{isl}}$ for arbitrary δV_{pl} , obtained for any $k_{\text{B}}T/E_{\text{C}}$ and by second order expansion in $\sqrt{1 - \tau}$ of the connected QPC. For $T \lesssim 30$ mK, this prediction given Supplementary Eq. 23 is effectively indiscernible from a second order expansion in $\pi^2 k_{\text{B}}T/E_{\text{C}}$:

$$\delta N_{\text{isl}} = \frac{\delta V_{\text{pl}}}{\Delta} + \frac{\gamma\sqrt{1-\tau}}{\pi} \left(1 - \frac{(\pi^2 k_{\text{B}}T)^2}{3E_{\text{C}}^2} \right) \sin \frac{2\pi\delta V_{\text{pl}}}{\Delta} + \frac{2\gamma^2(1-\tau)}{\pi^2} \left(1 - \frac{(\pi^2 k_{\text{B}}T)^2}{E_{\text{C}}^2} \right) \sin \frac{4\pi\delta V_{\text{pl}}}{\Delta}, \quad (4)$$

where $\gamma = \exp(C_{\text{E}}) \simeq 1.78107$ with $C_{\text{E}} \simeq 0.577216$ the Euler constant. The dashed lines in Fig. 2b represent $\delta N_{\text{isl}} - \delta V_{\text{pl}}/\Delta$, with δN_{isl} given by Supplementary Eq. 23, using the separately characterized values of T , $\tau = 0.985$ and $E_{\text{C}} = 39$ μeV .

From Eq. 4, one straightforwardly obtains for $\pi^2 k_{\text{B}}T/E_{\text{C}}, \sqrt{1 - \tau} \ll 1$ the charge analog of the zero-field magnetic susceptibility:

$$\frac{\chi}{(g\mu_{\text{B}})^2} \equiv \frac{\Delta}{2E_{\text{C}}} \frac{\partial N_{\text{isl}}}{\partial V_{\text{pl}}} (\delta V_{\text{pl}} = 0) \simeq \frac{1}{2E_{\text{C}}} \left[1 + 2\gamma\sqrt{1-\tau} + \frac{8}{\pi}\gamma^2(1-\tau) - \frac{(\pi^2 k_{\text{B}}T)^2}{E_{\text{C}}^2} \left(\frac{2}{3}\gamma\sqrt{1-\tau} + \frac{8}{\pi}\gamma^2(1-\tau) \right) \right]. \quad (5)$$

This expression together with the separately characterized T , τ and E_{C} gives the predictions displayed as continuous lines in Fig. 3. The T^2 approach to a low temperature fixed value of χ corresponds to the standard Kondo prediction¹ (see Eq. 7).

The theoretical expression of the Kondo temperature can be obtained by comparing Eq. 5 with the asymptotic spin Kondo prediction in the low temperature limit $\chi(T \ll T_{\text{K}}) \simeq n_{\text{w}}/4k_{\text{B}}T_{\text{K}}$, with $n_{\text{w}} \simeq 0.4107$ the Wilson number (see Eq. 7). This gives in the present $\sqrt{1 - \tau} \ll 1$ limit:

$$k_{\text{B}}T_{\text{K}} \simeq \frac{E_{\text{C}}n_{\text{w}}/2}{1 + 2\gamma\sqrt{1-\tau} + 8/\pi\gamma^2(1-\tau)}. \quad (6)$$

This expression for the Kondo temperature is represented as a red line in the inset of Fig. 4b. Note that it is not possible based on Eq. 5 to write $k_B T_K$ as a function of T/T_K beyond the linear term. This could be explained by the fact that, in the corresponding $\sqrt{1-\tau} \ll 1$ limit, the value of $k_B T_K$ is comparable to the high energy cutoff E_C thus giving rise to non-universal contributions beyond lowest order in temperature.

Universal Kondo predictions. In this section, we recapitulate some expressions used in the main text for the Kondo behavior of the susceptibility χ , the renormalization flow of the effective spin $k_B T_K \chi$ and its β -function, and the renormalization flow of the Kondo impurity magnetization vs $E_Z/k_B T_K$.

The magnetic susceptibility $\chi/(g\mu_B)^2 \equiv \partial \langle S_z \rangle / \partial (g\mu_B B)$ of a spin-1/2 Kondo impurity is predicted to asymptotically approach at low temperatures (see e.g. Ref. 1, Eqs. 4.58, 6.31, 6.79):

$$\frac{\chi(T \ll T_K)}{(g\mu_B)^2} = \frac{n_w}{4k_B T_K} \left(1 - \frac{\sqrt{3}}{4} \pi^3 n_w^2 \left(\frac{T}{T_K} \right)^2 + O\left(\frac{T}{T_K} \right)^4 \right), \quad (7)$$

with $n_w = \exp(C_E + 1/4)/\pi^{3/2} \simeq 0.4107$ the Wilson number. In the opposite limit of high temperatures with respect to T_K , the susceptibility reads (see e.g. Ref. 1, Eq. 3.53):

$$\frac{\chi(T \gg T_K)}{(g\mu_B)^2} = \frac{1}{4k_B T} \left(1 - \frac{1}{\log(T/T_K)} - \frac{\log(\log(T/T_K))}{2 \log^2(T/T_K)} + O(\log^{-2}(T/T_K)) \right). \quad (8)$$

The magnetic susceptibility coefficient (Curie constant) displayed in Fig. 4a,b is defined as $k_B T_K \chi / (g\mu_B)^2$. The theoretical asymptotic expression at low T/T_K displayed in Fig. 4b reads:

$$\frac{k_B T_K \chi(T \ll T_K)}{(g\mu_B)^2} \simeq \frac{n_w}{4} \frac{T}{T_K}. \quad (9)$$

The high temperature asymptotic prediction for the magnetic susceptibility coefficient (Curie constant) displayed in Fig. 4b is calculated by solving (see e.g. Ref. 1, Eqs. 4.51 and 4.52):

$$\Phi(2k_B T_K \chi / (g\mu_B)^2 - 1/2) = \log(T/T_K), \quad (10)$$

with the function $\Phi(x)$ given by:

$$\Phi(x) = 1/2x - \log|2x|/2 + 3.1648x + O(x^2). \quad (11)$$

Without the linear term in x in the above expression of Φ , solving Eq. 10 leads to the expression of χ given in Eq. 8. Including the linear term increases the range of validity in T/T_K of the asymptotic solution, allowing us to make contact with the numerical calculation available up to $T/T_K \approx 10^3$.

The theoretical β -function characterizing the renormalization flow of the magnetic susceptibility coefficient (Curie constant) is defined as $\beta \equiv \partial (k_B T_K \chi / (g\mu_B)^2) / \partial \log T$ as a function of $k_B T_K \chi / (g\mu_B)^2$. From Eq. 9, which is linear in T , the low T_K asymptote displayed as a dashed straight line in Fig. 4c is simply:

$$\beta(x \ll 1) \simeq x, \quad (12)$$

with $x \equiv k_B T_K \chi / (g\mu_B)^2$. From Eq. 8, keeping only the first two terms in the parenthesis, the asymptote near $k_B T_K \chi / (g\mu_B)^2 \approx 1/4$ displayed as a dashed line in Fig. 4c reads:

$$\beta(1/4 - x \ll 1) \simeq (1 - 4x)^2/4. \quad (13)$$

The full prediction shown as a continuous line in Fig. 4c is obtained by discrete differentiation of the numerical calculation (continuous line in Fig. 4b), averaged by Fourier filtering and completed by the asymptotic analytical predictions.

The magnetization of a Kondo impurity in the limit of low temperatures with respect to the Zeeman splitting ($k_B T \ll E_Z$, both small compared to the high energy cutoff) is predicted to follow a universal renormalization flow controlled by the parameter $E_Z/k_B T_K$, which is shown as a continuous line in Fig. 5a. This prediction can be expressed analytically, with a different equation depending on whether $x \equiv \frac{E_Z}{k_B T_K} \frac{\exp(C_E + 3/4)}{2\pi\sqrt{2}}$ is larger or smaller than 1 (see Eqs. 4.29c in Ref. 30, and Ref. 1 or the comparison with Eq. 7 at $x \ll 1$ for the numerical factor between x and $E_Z/k_B T_K$):

$$S_{\text{thy}}^{E_Z \gg T}(x > 1) = \frac{1}{2} - \frac{1}{2\pi^{3/2}} \int_0^\infty dt \frac{\sin(\pi t)}{t} e^{-t \ln t + t} x^{-2t} \Gamma(t + \frac{1}{2}),$$

$$S_{\text{thy}}^{E_Z \gg T}(x < 1) = \frac{1}{2\sqrt{\pi}} \sum_{k=0}^\infty (-1)^k \frac{(k + \frac{1}{2})^{k-1/2}}{k!} e^{-k-1/2} x^{2k+1}. \quad (14)$$

Data availability. The data used to produce the plots within this paper are available via Zenodo at <https://doi.org/10.5281/zenodo.10033055>. Source data are provided with this paper.

Code availability. The codes used to produce the plots within this paper are available via Zenodo at <https://doi.org/10.5281/zenodo.10033055>.

[1] Hewson, A. C. *The Kondo problem to heavy fermions* (Cambridge Univ. Press, 1997).
 [2] Cox, D. L. & Zawadowski, A. Exotic Kondo effects in metals: Magnetic ions in a crystalline electric field and tunnelling centres. *Adv. Phys.* **47**, 599–942 (1998).
 [3] Vojta, M. Impurity quantum phase transitions. *Phil. Mag.* **86**, 1807–1846 (2006).
 [4] Dzero, M., Sun, K., Galitski, V. & Coleman, P. Topological Kondo Insulators. *Phys. Rev. Lett.* **104**, 106408 (2010).
 [5] Emery, V. J. & Kivelson, S. Mapping of the two-channel Kondo problem to a resonant-level model. *Phys. Rev. B* **46**, 10812–10817 (1992).

[6] Lopes, P. L. S., Affleck, I. & Sela, E. Anyons in multichannel Kondo systems. *Phys. Rev. B* **101**, 085141 (2020).
 [7] Komijani, Y. Isolating Kondo anyons for topological quantum computation. *Phys. Rev. B* **101**, 235131 (2020).
 [8] Rajan, V., Lowenstein, J. & Andrei, N. Thermodynamics of the Kondo Model. *Phys. Rev. Lett.* **49**, 497–500 (1982).
 [9] Affleck, I. & Ludwig, A. W. W. Exact conformal-field-theory results on the multichannel Kondo effect: Single-fermion Green's function, self-energy, and resistivity. *Phys. Rev. B* **48**, 7297–7321 (1993).
 [10] Wilson, K. G. The renormalization group: critical phenomena and the Kondo problem. *Rev. Mod. Phys.* **47**,

- 773–840 (1975).
- [11] Goldhaber-Gordon, D. *et al.* Kondo effect in a single-electron transistor. *Nature* **391**, 156–159 (1998).
- [12] Cronenwett, S. M., Oosterkamp, T. H. & Kouwenhoven, L. P. A Tunable Kondo Effect in Quantum Dots. *Science* **281**, 540–544 (1998).
- [13] Babić, B., Kontos, T. & Schönenberger, C. Kondo effect in carbon nanotubes at half filling. *Phys. Rev. B* **70**, 235419 (2004).
- [14] Potok, R. M., Rau, I. G., Shtrikman, H., Oreg, Y. & Goldhaber-Gordon, D. Observation of the two-channel Kondo effect. *Nature* **446**, 167–171 (2007).
- [15] Sasaki, S., Amaha, S., Asakawa, N., Eto, M. & Tarucha, S. Enhanced Kondo Effect via Tuned Orbital Degeneracy in a Spin 1/2 Artificial Atom. *Phys. Rev. Lett.* **93**, 017205 (2004).
- [16] Mebrahtu, H. *et al.* Observation of Majorana Quantum Critical Behaviour in a Resonant Level Coupled to a Dissipative Environment. *Nat. Phys.* **9**, 732–737 (2013).
- [17] Felsch, W., Winzer, K. & Minnigerode, G. Magnetic Susceptibility of (La, Ce) A12 Alloys. *Z. Phys. B* **21**, 151–156 (1975).
- [18] Desjardins, M. M. *et al.* Observation of the frozen charge of a Kondo resonance. *Nature* **545**, 71–74 (2017).
- [19] Lebanon, E., Schiller, A. & Anders, F. B. Coulomb blockade in quantum boxes. *Phys. Rev. B* **68**, 041311 (2003).
- [20] Field, M. *et al.* Measurements of Coulomb blockade with a noninvasive voltage probe. *Phys. Rev. Lett.* **70**, 1311 (1993).
- [21] Rössler, C. *et al.* Tunable charge detectors for semiconductor quantum circuits. *New J. Phys.* **15**, 033011–033023 (2013).
- [22] Baer, S. & Ensslin, K. *Transport Spectroscopy of Confined Fractional Quantum Hall Systems* (Springer Cham, 2015). URL <https://doi.org/10.1007/978-3-319-21051-3>.
- [23] Hartman, N. *et al.* Direct entropy measurement in a mesoscopic quantum system. *Nat. Phys.* **14**, 1083–1086 (2018).
- [24] Berman, D., Zhitenev, N. B., Ashoori, R. C. & Shayegan, M. Observation of Quantum Fluctuations of Charge on a Quantum Dot. *Phys. Rev. Lett.* **82**, 161–164 (1999).
- [25] David S., D., Carol, L., Robert M., W., Kevin D., M. & Gossard, A. C. Direct measurement of the destruction of charge quantization in a single-electron box. *Applied Physics Letters* **74**, 1045–1047 (1999).
- [26] Lehnert, K. W. *et al.* Quantum Charge Fluctuations and the Polarizability of the Single-Electron Box. *Phys. Rev. Lett.* **91**, 106801 (2003).
- [27] Iftikhar, Z. *et al.* Two-channel Kondo effect and renormalization flow with macroscopic quantum charge states. *Nature* **526**, 233–236 (2015).
- [28] Iftikhar, Z. *et al.* Tunable quantum criticality and superballistic transport in a ‘charge’ Kondo circuit. *Science* **360**, 1315–1320 (2018).
- [29] Pouse, W. *et al.* Quantum simulation of an exotic quantum critical point in a two-site charge Kondo circuit (2021). ArXiv: 2108.12691 (Nat. Phys., to be published).
- [30] Andrei, N., Furuya, K. & Lowenstein, J. H. Solution of the Kondo problem. *Rev. Mod. Phys.* **55**, 331–402 (1983).
- [31] Matveev, K. A. Quantum fluctuations of the charge of a metal particle under the Coulomb blockade conditions. *Sov. Phys. JETP* **72**, 892–899 (1991).
- [32] Matveev, K. A. Coulomb blockade at almost perfect transmission. *Phys. Rev. B* **51**, 1743–1751 (1995).
- [33] Jezouin, S. *et al.* Controlling charge quantization with quantum fluctuations. *Nature* **536**, 58–62 (2016).
- [34] Sivre, E. *et al.* Heat Coulomb blockade of one ballistic channel. *Nat. Phys.* **14**, 145–148 (2018).
- [35] Glazman, L. I. & Raikh, M. E. Resonant Kondo Transparency of a Barrier with Quasilocally Impurity States. *JETP Lett.* **47**, 452–455 (1988).
- [36] Ng, T. K. & Lee, P. A. On-Site Coulomb Repulsion and Resonant Tunneling. *Phys. Rev. Lett.* **61**, 1768–1771 (1988).
- [37] Nozières, P. & Blandin, A. Kondo effect in real metals. *J. Phys.* **41**, 193–211 (1980).
- [38] Mitchell, A. K., Landau, L. A., Fritz, L. & Sela, E. Universality and Scaling in a Charge Two-Channel Kondo Device. *Phys. Rev. Lett.* **116**, 157202 (2016).
- [39] Sela, E. *et al.* Detecting the Universal Fractional Entropy of Majorana Zero Modes. *Phys. Rev. Lett.* **123**, 147702 (2019).
- [40] Han, C. *et al.* Fractional Entropy of Multichannel Kondo Systems from Conductance-Charge Relations. *Phys. Rev. Lett.* **128**, 146803 (2022).
- [41] Bayat, A., Sodano, P. & Bose, S. Negativity as the entanglement measure to probe the Kondo regime in the spin-chain Kondo model. *Phys. Rev. B* **81**, 064429 (2010).
- [42] Kim, D., Shim, J. & Sim, H.-S. Universal Thermal Entanglement of Multichannel Kondo Effects. *Phys. Rev. Lett.* **127**, 226801 (2021).
- [43] George, M., Steve, C. & Andrew K., M. Thermometry of strongly correlated fermionic quantum systems using impurity probes. *Physical Review A* **107**, 042614 (2023).
- [44] Iftikhar, Z. *et al.* Primary thermometry triad at 6 mK in mesoscopic circuits. *Nat. Commun.* **7**, 12908 (2016).
- [45] Jezouin, S. *et al.* Quantum Limit of Heat Flow Across a Single Electronic Channel. *Science* **342**, 601–604 (2013).
- [46] Grabert, H. Charge fluctuations in the single-electron box: Perturbation expansion in the tunneling conductance. *Phys. Rev. B* **50**, 17364–17377 (1994).

Acknowledgments. This work was supported by the European Research Council (ERC-2020-SyG-951451), the French National Research Agency (ANR-18-CE47-0014-01) and the French RENATECH network. We thank K. Ensslin, J. Folk and A. Mitchell for discussions.

Author Contributions Statement. C.P. performed the experiment with inputs from A.Aa., A.An., F.P. and P.G.; C.P., A.An. and F.P. analyzed the data; C.P., A.Aa and F.P. fabricated the sample; A.C. and U.G. grew the 2DEG; C.H., E.S. and Y.M. developed the theory; C.P. and F.P. wrote the paper with inputs from all authors; A.An. and F.P. led the project.

Competing Interests Statement. The authors declare no competing interests. Correspondence and requests for materials should be addressed to A.An. (anne.anthore@c2n.upsaclay.fr) and F.P. (frederic.pierre@cnsr.fr).

Supplementary Information: Observing the universal screening of a Kondo impurity

In this supplementary information, we establish the analytical expressions for δN_{isl} and the corresponding susceptibility as presented in Eqs. (4,5) of the main manuscript. Additionally, we provide the non-perturbative expression for δN_{isl} and the associated susceptibility in terms of T/E_C , which is used in Fig. 2b and Fig. 3. Finally, we show and compare with asymptotic predictions the measured charge susceptibility versus transmission probability across the QPC, which provides a complementary view point with respect to $\chi(T)$ displayed in Fig. 3.

I. DERIVATION OF EQS. (4,5) IN MAIN MANUSCRIPT

We consider a metallic island whose electrostatic energy can be controlled thanks to a plunger gate nearby as

$$E_{\text{isl}} = \frac{(eN_{\text{isl}} - eN_g)^2}{2C_0}. \quad (1)$$

Here, N_{isl} represents the number of electrons inside the island, $N_g = V_{\text{pl}}/\Delta$ denotes the normalized gate voltage, and $2C_0$ represents the capacitance of the metallic island. This capacitance also determines the charging energy of the island, which is the energy required to add an electron to it. When $N_g = n + \frac{1}{2}$, both the states $N_{\text{isl}} = n$ and $n + 1$ possess the same energy, thus defining the pseudo-spin of the metallic island. Taking this point as a reference for Kondo mapping by setting $\delta V_{\text{pl}} = 0$, the relevant parameter becomes $\delta N_{\text{isl}} = N_{\text{isl}}(\delta V_{\text{pl}}) - N_{\text{isl}}(0)$.

The Coulomb blockade phenomenon diminishes as the coupling to an electron bath increases. When the tunnel barrier τ approaches 1, quantum charge fluctuations disrupt the charge quantization, leading to the absence of Coulomb blockade. Thus, in this regime of strong coupling with only one electron bath, a theoretical framework is needed to characterize the state of the island.

Following Matveev¹, we can treat the system composed of the metallic island and the connected quantum Hall channel as one-dimensional. Furthermore, the typical energy scale at which Coulomb blockade becomes significant, denoted by $E_C (= 1/2C_0)$, is much smaller than the Fermi energy, allowing for the utilization of bosonization techniques. At low energies, the electron system can be regarded as an elastic medium, enabling the definition of two chiral boson fields, ϕ_u and ϕ_d . The Hamiltonian describing the system with Coulomb interaction and back-scattering becomes $H = H_0 + H_B$ where

$$\begin{aligned} H_0 &= \int \frac{dx}{4\pi} [(\partial_x \phi_u)^2 + (\partial_x \phi_d)^2] + \frac{E_C}{4\pi^2} (\phi_u(0) - \phi_d(0))^2 - 2E_C N_g \frac{1}{2\pi} (\phi_u(0) - \phi_d(0)), \\ H_B &= -\frac{Dr}{2\pi} (e^{i(\phi_u(0) - \phi_d(0))} + e^{-i(\phi_u(0) - \phi_d(0))}). \end{aligned} \quad (2)$$

Here we set $\hbar = e = k_B = v_F = 1$. D is the bandwidth of the system, and $r = \sqrt{1 - \tau}$ is the back-scattering coefficient. The sign of the back-scattering coefficient is negative following the convention of Eq. (18) in Ref. 1. The bosonic fields satisfy the commutation relations $[\phi_i(x), \phi_j(y)] = i\delta_{ij}\pi \text{sgn}(x - y)$. The occupation number of the metallic dot at temperature T , measured from the charge degeneracy point, is obtained from the partition function Z of the system,

$$\delta N_{\text{isl}} = \frac{T}{2E_C} \frac{1}{Z} \frac{\partial Z}{\partial N_g} - \frac{1}{2}. \quad (3)$$

To calculate δN_{isl} up to the second order of r , we begin by deriving the partition function using the former boson fields. Initially, we transform these fields into the displacement mode of the elastic medium, denoted as $\phi_C = \frac{1}{\sqrt{2}}(\phi_u - \phi_d)$, along with its corresponding momentum mode, $\phi_I = \frac{1}{\sqrt{2}}(\phi_u + \phi_d)$. The charge of the island is simply given by the displacement at the position of the constriction, $\phi_C(0)$. Consequently, ϕ_I is decoupled from our physical observable of interest, and we solely consider ϕ_C in our analysis. The Lagrangian for the ϕ_C mode is given by $\mathcal{L} = \mathcal{L}_0 + \mathcal{L}_B$, where

$$\mathcal{L}_0 = \frac{v_F}{4\pi} \int dx \partial_x \phi_C (\partial_t - \partial_x) \phi_C - \frac{E_C}{2\pi^2} (\phi_C(0) - \sqrt{2\pi} N_g)^2, \quad \mathcal{L}_B = \frac{Dr}{2\pi} (e^{i\sqrt{2}\phi_C(0)} + e^{-i\sqrt{2}\phi_C(0)}). \quad (4)$$

Note that the electrostatic part (the two last terms of \mathcal{L}_0) is now quadratic in bosonic variables and can be treated exactly. Moreover the back-scattering part \mathcal{L}_B has the form of a cosine, leading to a periodic dependence with N_g .

Fourier transforming the boson field as

$$\phi(x, \tau') = \sqrt{\frac{T}{L}} \sum_{\omega_n, q} \phi(q, \omega_n) e^{iqx - i\omega_n \tau'}, \quad \phi(\tau') = \sqrt{T} \sum_{\omega_n} \phi(\omega_n) e^{-i\omega_n \tau'}, \quad (5)$$

with $\omega_n = 2\pi T n$, $\tau' = it$, and system size L , the partition function becomes

$$Z = \int \mathcal{D}\phi_C(x, \tau') \exp[-\mathcal{S}(\phi_C)], \quad (6)$$

where

$$\mathcal{S} = \sum_{\omega_n, q} \frac{q(q - i\omega_n)}{4\pi} \phi_C(q, \omega_n) \phi_C(-q, -\omega_n) + \int_0^{1/T} d\tau' \frac{E_C}{2\pi^2} (\phi_C(0, \tau') - \sqrt{2\pi} N_g)^2 + \frac{Dr}{2\pi} (e^{i\sqrt{2}\phi_C(0, \tau')} + e^{-i\sqrt{2}\phi_C(0, \tau')}). \quad (7)$$

To compute δN_{isl} , we expand Eq. (6) in powers of r up to r^2 order, as $Z = Z_0(1 + Z_1 + Z_2 + \dots)$. At zeroth order of r , the contribution of the gate on the island charge is simply linear, as it is computed from $\frac{1}{Z_0} \frac{\partial Z_0}{\partial N_g} = \frac{2E_C}{T} N_g$. Indeed, at $\tau = 1$ the charge fluctuations completely vanishes and so does the Kondo effect. Up to second order, δN_{isl} can be written as

$$\delta N_{\text{isl}} \simeq \frac{T}{2E_C} \frac{1}{Z_0} \frac{\partial Z_0}{\partial N_g} + \frac{T}{2E_C} \frac{1}{1 + Z_1 + Z_2} \frac{d(1 + Z_1 + Z_2)}{dN_g} - \frac{1}{2} \simeq N_g - \frac{1}{2} + \frac{T}{2E_C} \frac{dZ_1}{dN_g} - \frac{T}{2E_C} Z_1 \frac{dZ_1}{dN_g} + \frac{T}{2E_C} \frac{dZ_2}{dN_g}. \quad (8)$$

Below we compute Z_1 and Z_2 as a function of N_g .

The first order correction, Z_1 is

$$Z_1 = \frac{Dr}{2\pi} \frac{1}{Z_0} \sum_{\zeta=\pm 1} \int_0^{1/T} d\tau' \int \mathcal{D}\phi_C \exp \left[\sum_{\omega_n} -\frac{|\omega_n| + E_C/\pi}{2\pi} |\phi_C(\omega_n)|^2 + i\sqrt{2T}\zeta e^{i\omega_n \tau'} \phi_C(\omega_n) + \frac{E_C N_g}{\pi\sqrt{T/2}} \phi_C(0) \right]. \quad (9)$$

First we perform the Gaussian integration over ϕ_C . After integrating out ϕ_C and τ , we obtain

$$Z_1 = \frac{Dr}{2\pi} \frac{1}{T} \sum_{\zeta} \exp \left[-\sum_{\omega_n} \frac{\pi T}{|\omega_n| + E_C/\pi} - \frac{\pi^2}{E_C} T + 2i\pi N_g \zeta \right] \quad (10)$$

It is important to emphasize that this expression is not limited to small values of T/E_C . The temperature can be increased as long as the thermal energy scale remains smaller than the fermi energy. For now we will focus on the regime where $T/E_C \ll 1$ to derive analytical results, but in Sec. II we will evaluate the sum exactly. Then we may replace the following sum by

$$\pi T \sum_{\omega_n} \frac{e^{-|\omega_n|/D}}{|\omega_n| + E_C/\pi} = \log \left(\frac{D}{2\gamma\pi T} \right) - \psi \left(1 + \frac{E_C}{2\pi^2 T} \right) \simeq \log \left[\frac{\pi D}{\gamma E_C} \right] - \frac{\pi^2 T}{E_C} + \frac{\pi^4 T^2}{3E_C^2}; \quad (11)$$

see Eq. (A6b) in Ref. 1. Here $\gamma = e^{\mathbf{C}}$, where $\mathbf{C} \simeq 0.5772$ is the Euler's constant. The partition function therefore is

$$Z_1 = 2\gamma r \cos(2\pi N_g) \exp \left[\psi \left(1 + \frac{E_C}{2\pi^2 T} \right) - \frac{\pi^2}{E_C} T \right] \simeq \frac{\gamma r E_C}{\pi^2 T} \cos(2\pi N_g) \exp \left[-\frac{\pi^4}{3E_C^2} T^2 \right]. \quad (12)$$

This first result gives the first order correction to the linear dependence with N_g , recovering the periodic behaviour due to the finite charging energy and the other charge states available.

Next we compute the second order correction Z_2 ,

$$Z_2 = \frac{1}{2} \frac{D^2 r^2}{4\pi^2} \frac{1}{Z_0} \sum_{\zeta_{1,2}=\pm 1} \int_0^{1/T} d\tau_1 \int_0^{1/T} d\tau_2 \int \mathcal{D}\phi_C \exp \left[\sum_{\omega_n} -\frac{|\omega_n| + E_C/\pi}{2\pi} |\phi_C(\omega_n)|^2 + i\sqrt{2T}(\zeta_1 e^{i\omega_n \tau_1} + \zeta_2 e^{i\omega_n \tau_2}) \phi_C(\omega_n) + \frac{E_C N_g}{\pi\sqrt{T/2}} \phi_C(0) \right]. \quad (13)$$

The factor of $1/2$ in front originates from the expansion of r^2 . After integrating out the ϕ_C field, we obtain

$$Z_2 = \frac{D^2 r^2}{8\pi^2} \sum_{\zeta_{1,2}} \int_0^{1/T} d\tau_1 d\tau_2 \exp \left[\sum_{\omega_n} -\frac{2\pi T [1 + \zeta_1 \zeta_2 \cos(\omega_n(\tau_1 - \tau_2))]}{|\omega_n| + E_C/\pi} - \frac{2\pi^2 T}{E_C} (1 + \zeta_1 \zeta_2) + 2i\pi N_g (\zeta_1 + \zeta_2) \right]. \quad (14)$$

Using the same approximation than above for the summation which is valid for $T/E_C \ll 1$ and $0 \ll \tau' \ll 1/T$, it results in

$$\sum_{\omega_n} \frac{2\pi T e^{-|\omega_n|/D}}{|\omega_n| + E_C/\pi} \cos(\omega_n \tau') \simeq -\frac{2\pi^2 T}{E_C} + \frac{2\pi^4 T^2}{E_C^2} \frac{1}{\sin^2(\pi T \tau')}. \quad (15)$$

Now we only consider the N_g dependent part and change the variables as $\tau_a = \tau_1 + \tau_2$ and $\tau_b = \tau_1 - \tau_2$. This transformation comes with a $1/4$ Jacobian. Thanks to the former approximation, Z_2 becomes

$$Z_2 \simeq \frac{E_C^2 \gamma^2 r^2}{8\pi^4} \exp \left[-\frac{2\pi^4 T^2}{3E_C^2} \right] 2 \cos(4\pi N_g) \frac{1}{T} \int_0^{1/T} d\tau_b \exp \left[-\frac{2\pi^4 T^2}{E_C^2} \frac{1}{\sin^2(\pi T \tau_b)} \right]. \quad (16)$$

For $0 < \tau_b < \pi/E_C$, or $1/T - \pi/E_C < \tau_b < 1/T$, the integrand becomes negligible. Hence we neglect these parts and focus on $\pi/E_C < \tau_b < 1/T - \pi/E_C$, where the partition function can be approximated by

$$Z_2 \simeq \frac{E_C^2 \gamma^2 r^2}{4\pi^4 T} \cos(4\pi N_g) \exp \left[-\frac{2\pi^4 T^2}{3E_C^2} \right] \int_{\pi/E_C}^{1/T - \pi/E_C} d\tau_b \left[1 - \frac{2\pi^4 T^2}{E_C^2} \frac{1}{\sin^2(\pi T \tau_b)} \right], \quad (17)$$

Noting that

$$\int_{\pi/E_C}^{1/T - \pi/E_C} d\tau_b \frac{1}{\sin^2(\pi T \tau_b)} = \frac{2 \cot(\pi^2 T/E_C)}{\pi T} \simeq \frac{2E_C}{\pi^3 T^2} - \frac{2\pi}{3E_C}, \quad (18)$$

we obtain Z_2 as

$$Z_2 \simeq \frac{E_C^2 \gamma^2 r^2}{8\pi^4 T} \cos(4\pi N_g) \exp \left[-\frac{2\pi^4 T^2}{3E_C^2} \right] \left[\frac{2}{T} - \frac{2\pi^4 T^2}{E_C^2} \left(\frac{4E_C}{\pi^3 T^2} - \frac{4\pi}{3E_C} \right) \right]. \quad (19)$$

Finally, from the derivation of Z_0 , Z_1 and Z_2 , we can compute the total contribution to the number of electron inside the island up to $(T/E_C)^2$ order and r^2 order (with $r = \sqrt{1 - \tau}$ and $N_g = V_{pl}/\Delta$),

$$\delta N_{\text{isl}} \simeq \frac{\delta V_{pl}}{\Delta} + \frac{\gamma \sqrt{1 - \tau}}{\pi} \left[1 - \frac{1}{3} \frac{\pi^4 T^2}{E_C^2} \right] \sin \frac{2\pi \delta V_{pl}}{\Delta} + \frac{2\gamma^2 (1 - \tau)}{\pi^2} \left[1 - \frac{\pi^4 T^2}{E_C^2} \right] \sin \frac{4\pi \delta V_{pl}}{\Delta}. \quad (20)$$

For $T = 0$ and at the 1st order of r , the above equation coincides with Eq. (25) in Ref 1. This study extended the previously mentioned findings to higher orders of reflections and non-zero temperature, enabling a direct comparison with the experimental data. The charge susceptibility χ at $\delta V_{pl} = 0$ is

$$\frac{\chi}{(g\mu_B)^2} = \frac{\Delta}{2E_C} \frac{\partial N_{\text{isl}}}{\partial V_{pl}} \simeq \frac{1}{2E_C} \left[1 + 2\gamma \sqrt{1 - \tau} + \frac{8\gamma^2 (1 - \tau)}{\pi} - \frac{(\pi T)^2}{(E_C/\pi)^2} \left(\frac{2\gamma \sqrt{1 - \tau}}{3} + \frac{8\gamma^2 (1 - \tau)}{\pi} \right) \right]. \quad (21)$$

In the main text, this quantity is compared to Kondo predictions. While we observe a T^2 dependence as expected for a Kondo system, it cannot be expressed as a universal function of T/T_K beyond the linear term. This is due to the fact that the Kondo temperature T_K can become quite large as τ approaches one, leading to non-universal contributions beyond the lowest-order in temperature.

II. EXPRESSION FOR FIG. 2B

Here we provide the exact expression of δN_{isl} up to r^2 orders, but valid for arbitrary T/E_C . To obtain the exact result, we use the relations

$$2\pi T \sum_{\omega_n} \frac{e^{-|\omega_n|/D}}{|\omega_n| + E_C/\pi} = -2 \log \left(\frac{2\gamma \pi T}{D} \right) - 2\psi \left(1 + \frac{E_C}{2\pi^2 T} \right), \quad (22)$$

$$2\pi T \sum_{\omega_n} \frac{e^{-|\omega_n|/D}}{|\omega_n| + E_C/\pi} \cos(\omega_n \tau') = \frac{4\pi^2 T}{E_C + 2\pi^2 T} \text{Re} \left[e^{2i\pi T \tau'} {}_2F_1 \left(1, \frac{E_C}{2\pi^2 T} + 1; \frac{E_C}{2\pi^2 T} + 2; e^{2i\pi T \tau'} \right) \right].$$

Here ${}_2F_1(a, b; c; z)$ is the hypergeometric function. Therefore δN_{isl} is

$$\begin{aligned} \delta N_{\text{isl}} = & \frac{\delta V_{\text{pl}}}{\Delta} + \frac{2\pi T}{E_C} \gamma \sqrt{1-\tau} \exp\left[\psi\left(1 + \frac{E_C}{2\pi^2 T}\right) - \frac{\pi^2 T}{E_C}\right] \sin \frac{2\pi \delta V_{\text{pl}}}{\Delta} \\ & + \frac{2\pi T}{E_C} \gamma^2 (1-\tau) \exp\left[2\psi\left(1 + \frac{E_C}{2\pi^2 T}\right) - \frac{2\pi^2 T}{E_C}\right] \sin \frac{4\pi \delta V_{\text{pl}}}{\Delta} \\ & \times \left(1 - T \exp\left[-\frac{2\pi^2 T}{E_C}\right] \int_0^{1/T} d\tau' \exp\left[-\frac{2}{1 + \frac{E_C}{2\pi^2 T}} \text{Re}\left[e^{2i\pi T \tau'} {}_2F_1\left(1, \frac{E_C}{2\pi^2 T} + 1; \frac{E_C}{2\pi^2 T} + 2; e^{2i\pi T \tau'}\right)\right]\right]\right). \end{aligned} \quad (23)$$

This is this expression that is used in Fig. 2b of the main text and from which we can extract the susceptibility predictions for Fig. 3.

III. CHARGE PSEUDOSPIN SUSCEPTIBILITY VERSUS TRANSMISSION PROBABILITY

In Fig. 3 of the main manuscript, the charge pseudospin susceptibility is displayed versus temperature, with different symbols corresponding to different tunings of the transmission probability τ of the connected QPC. Here, in Supplementary Fig. S1, we display the same charge susceptibility measurements now as a function of τ with different symbols and colors corresponding to different settings of the temperature up to $T \simeq 69$ mK. As further described below, the dashed and continuous lines correspond to the asymptotic predictions for our system at small and large τ , respectively.

The theoretical prediction in the strong coupling limit $1-\tau \ll 1$ shown as two continuous black lines in Supplementary Fig. S1 are straightforwardly obtained from $\frac{\chi}{(g\mu_B)^2} = \frac{\Delta}{2E_C} \frac{\partial \delta N_{\text{isl}}}{\partial V_{\text{pl}}}$ with δN_{isl} given in Eq. (23). The lower and higher curves correspond to $T = 9.4$ mK and 69.7 mK, respectively. Note that the comparison is without any fit parameters.

The theoretical predictions in the weak/tunnel coupling limit $\tau \ll 1$ are displayed as dashed lines with a color code corresponding to the indicated experimental temperature, without any free parameters. Following Ref. 2, the plotted predictions of Ref. 3 including perturbative Kondo corrections are given by:

$$\frac{\chi}{(g\mu_B)^2} = \frac{1}{4k_B T} \left(1 - 2\frac{\tau}{4\pi^2} \left(5.154 + \ln \frac{E_C}{\pi k_B T}\right)\right) + O\left[\tau^2, \frac{k_B T}{E_C}\right] \quad (24)$$

with $(g\mu_B)^2 = 2E_C$.

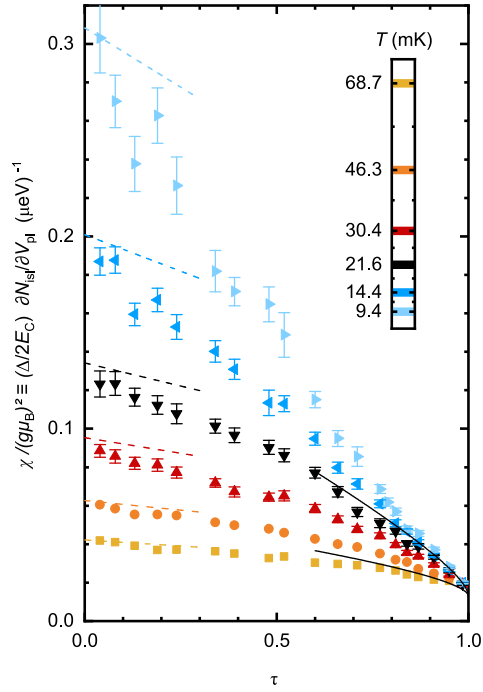


Figure S1. Charge pseudospin susceptibility versus transmission probability. The measured charge susceptibility at degeneracy ($\delta V_{pl} \approx 0$) is plotted as a function of the transmission probability τ across the QPC connected to the island. Solid black lines represent the quantitative predictions for the strong-coupling regime ($1 - \tau \ll 1$), computed for both the highest and lowest experimental temperatures (see Supplementary Section III). Dashed colored lines display the quantitative predictions in the weak-coupling/tunnel regime ($\tau \ll 1$) as given by Supplementary Eq. 24 at the experimental temperature indicated by the color code.

-
- [1] K. A. Matveev, Coulomb blockade at almost perfect transmission, Phys. Rev. B **51**, 1743 (1995).
 - [2] K. W. Lehnert, B. A. Turek, K. Bladh, L. F. Spietz, D. Gunnarsson, P. Delsing, and R. J. Schoelkopf, Quantum charge fluctuations and the polarizability of the single-electron box, Phys. Rev. Lett. **91**, 106801 (2003).
 - [3] H. Grabert, Charge fluctuations in the single-electron box: Perturbation expansion in the tunneling conductance, Phys. Rev. B **50**, 17364 (1994).